Journal of Applied Physics

Quantum tunneling between bent semiconductor nanowires

Cite as: J. Appl. Phys. **118**, 174301 (2015); https://doi.org/10.1063/1.4934646
Submitted: 22 September 2015 . Accepted: 10 October 2015 . Published Online: 02 November 2015

A. A. Sousa, Andrey Chaves, T. A. S. Pereira, G. A. Farias, and F. M. Peeters

JOURNAL OF APPLIED PHYSICS **118**, 174301 (2015)

Quantum tunneling between bent semiconductor nanowires

A. A. Sousa,[1,2,3,a)] Andrey Chaves,[1,b)] T. A. S. Pereira,[3,c)] G. A. Farias,[1,d)] and F. M. Peeters[2,1,e)]
[1]*Departamento de Física, Universidade Federal do Ceará, Caixa Postal 6030, Campus do Pici, 60455-900 Fortaleza, Ceará, Brazil*
[2]*Department of Physics, University of Antwerp, Groenenborgerlaan 171, B-2020 Antwerp, Belgium*
[3]*Instituto de Física, Universidade Federal de Mato Grosso, 78060-900, Cuiabá, Mato Grosso, Brazil*

(Received 22 September 2015; accepted 10 October 2015; published online 2 November 2015)

We theoretically investigate the electronic transport properties of two closely spaced L-shaped semiconductor quantum wires, for different configurations of the output channel widths as well as the distance between the wires. Within the effective-mass approximation, we solve the time-dependent Schrödinger equation using the split-operator technique that allows us to calculate the transmission probability, the total probability current, the conductance, and the wave function scattering between the energy subbands. We determine the maximum distance between the quantum wires below which a relevant non-zero transmission is still found. The transmission probability and the conductance show a strong dependence on the width of the output channel for small distances between the wires. © *2015 AIP Publishing LLC*. [http://dx.doi.org/10.1063/1.4934646]

I. INTRODUCTION

Advances in the fabrication and nanostructuring of semiconductor compounds opens up opportunities for combination of different shapes of devices on a nanometric scale.[1–4] There are numerous experimental methods and techniques of fabricating these semiconductor nanostructures, such as self-organized growth in a MBE chamber,[5–7] split-gate technique used to fabricate narrow quantum channels for electrons,[8] and AFM lithography, which can be used to create different nanostructures.[9,10] On a nanometric scale, transport properties of one-dimensional structures are of great interest and a large number of novel phenomena have been predicted and observed in recent years.[11,12] Here, we shall mention, for example, investigations on the transport properties through confined states in a 1D wire were performed by Auslaender *et al.*[13] Tserkovnyak *et al.*[14] gave a detailed experimental investigation and theoretical explanation of a set of interference patterns in the nonlinear tunneling conductance between two parallel wires that were first reported by Auslaender in 2002.[15]

From a theoretical point of view, the attempt to model increasingly smaller semiconductor systems that is driven by the miniaturization of technological devices has led to more systematic studies with the aim to describe in more detail the different physical effects, such as tunneling in transistor gate oxides[16,17] and energy quantization in nanometer scale MOSFETs.[18,19] In addition, different systems used to calculate the scattering probabilities per unit of time under the effect of perturbative potentials have been proposed and investigated. Some cases of interest here are those when adding an extra path in the system,[20] an effective potential simulating a Scanning Gate Microscopy tip[21,22] as well as the effect of a smooth potential in path's connections.[23]

In this work, we investigate the wave packet scattering in two L-shaped quantum wires (QWs) separated by a distance W_2, see Fig. 1. The aim is to find the minimum separation distance between two bent wires with acceptable values for tunneling. For this purpose, we inject a Gaussian wave packet in the left-lead and calculate the transmission into the bottom lead and the tunnelling into the second wire. Our theoretical model is based on the solution of the time dependent Schrödinger equation within the effective mass approach using the split-operator technique.[23,25] We consider different values of the wave packet kinetic energy and W_2 distances between the quantum wires as well as different width values for the second wire L. We then analyse how the conductivity depends on these parameters (W_2 and L).

This remainder of this organized as follows: In Sec. II, we describe our theoretical model and numerical technique to solve the time-dependent Schrödinger equation. In Sec. III, we discuss the transport properties of the system and we present our conclusions in Sec. IV.

II. THEORETICAL MODEL

Our model describes electrons in the (x, y) plane moving from left to right in a region with a L-shaped wire (see left side of Fig. 1). The effective-mass approximation was considered and all electrons are confined by a step like potential, i.e., $V(x,y) = 0$ inside the QW and $V(x, y) = V_0$ otherwise. Abrupt interfaces between the confinement region and the potential barrier are assumed. Similarly, in the right side of our set up, another L-shaped QW is considered. The left QW is assumed to have fixed width $W_1 = 10$ nm, whereas for right QW, three different widths L ($=W_1/2$, W_1, and $2W_1$). The smooth edges of the QWs are drawn by circles of radius $R_W = W_1/2$ and $R_L = L/2$ for the left and right wires, respectively, in order to approach more realistic systems.

[a)]Electronic address: ariel@fisica.ufc.br
[b)]Electronic address: andrey@fisica.ufc.br
[c)]Electronic address: teldo@fisica.ufmt.br
[d)]Electronic address: gil@fisica.ufc.br
[e)]Electronic address: francois.peeters@uantwerpen.be

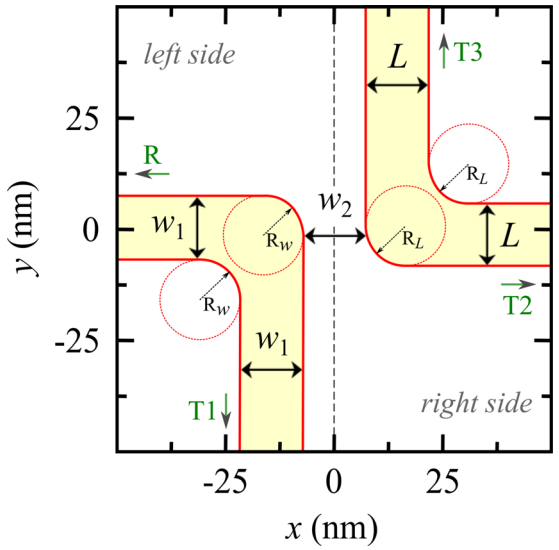

FIG. 1. Potential profile scheme for the QWs studied in this work. The two QWs are separated from each other by a distance W_2, ranging from 0 to 4.8 nm. The smooth connections between vertical and horizontal wire are described by circles of radius $R_W = W_1/2$ and $R_L = L/2$.

The left side is separated from the right by a distance W_2 which ranges from 0 nm to 4.8 nm in this work. We assume that the electron is always in the conduction band, and inelastic scattering events, or conduction-to-valence band transitions, are negligible, which is a reasonable approximation when dealing with low-temperature systems.

In the transverse cross section, the QW behaves as a quasi-one-dimensional channel where an electron confined in this region has a subband energy

$$E_n(k_x) = E_n^{(y)} + \frac{\hbar^2 k_x^2}{2m_e}, \tag{1}$$

where $E_n^{(y)}$ are the y components of the eigenvalues which were obtained numerically for a potential of $V_0 = 600$ meV. These eigenvalues are lower than the corresponding eigenvalues calculated for an infinite potential, $E_n^{(y)} = n^2\pi^2\hbar^2/2m_eW_1^2$, although this analytical expression can be used for an estimate of energies in a quantum well of W_1 width. A combination of a Gaussian function with a plane wave is injected from the left to the right along the x direction, so that at $t = 0$, the wave packet is given by

$$\Psi(x,y) = \exp\left[ik_0x - \frac{(x-x_0)^2}{2\sigma_x^2}\right]\phi_0(y). \tag{2}$$

Here, $k_0 = \sqrt{2m_e\varepsilon}/\hbar$ is a wave vector corresponding to the kinetic energy ε, and $\phi_0(y)$ is the ground state wave function of the quantum well in the y direction. The width of the wave packet in the x direction is fixed by σ_x. The time evolution of the wave packet is studied with the split-operator technique, which allows to separate the kinetic terms for each direction. This separation is important for systems with many degrees of freedom. We follow the approach of Refs. 23–26, whose details will not be reproduced here. Time evolution of wave packets describing conduction band electrons has been widely used as an important tool for understanding transport properties of low-dimensional systems,[27] and has proven to successfully reproduce experimental results fairly well.[28] Connection between time evolution methods and the Greens functions formalism can be seen in more detail, e.g., in Ref. 29.

The (x, y)-plane is discretized by a squared grid $\Delta x = \Delta y = 0.4$ nm, and the finite difference scheme is used to solve the derivatives in the kinetic energy terms of the Hamiltonian. To avoid spurious reflection when the wave packet reaches the edges of our set up, we applied an imaginary potential, as discussed in Ref. 23 and suggested by Manolopoulos.[31] The current of the system is given by

$$\mathbf{J} = -\frac{i\hbar}{2m_e}(\Psi^*\nabla\Psi - \Psi\nabla\Psi^*). \tag{3}$$

The transmission probabilities are calculated in three different positions at vertical (T_1 and T_3) and horizontal (T_2) axes, as shown in Fig. 1. For the horizontal axis, we fixed a point x_r, localized in the right side and the transmission T_2 is calculated as

$$T = \int_0^\infty dt \int_{-\infty}^{\infty} dy J_x(x_r, y, t). \tag{4}$$

For vertical axis, we fixed a point y_B in the bottom wire and a point y_T in the top wire and calculated the transmission T_1 and T_3 through Eq. (4), changing $J_x(x_r, y, t)$ for $J_y(x, y_T, t)$ and $J_y(x, y_B, t)$, respectively, and the above spatial integral is now evaluated along x-direction. The reflection probability R is calculated by fixing a point x_l in the left side and evaluating the integrals in dt and dy. More precisely,

$$R = -\int_0^\infty dt \int_{-\infty}^{\infty} dy J_x(x_L, y, t), \tag{5}$$

where J_x is the x component of the probability current.

In order to investigate the scattering of an electron into different subbands of the wires, we project the wave function on the j-th eigenstate of the quantum well at a fixed point x_i, using the relation

$$P_j(x_i, t) = |\langle\Psi|\phi_j\rangle|^2 = \left|\int_{-\infty}^{+\infty} dy\Psi(x_i, y, t)\phi_j(y)\right|^2. \tag{6}$$

Equation (6) is the probability density of finding an electron in the j-th subband at position x_i per length in the x direction. Moreover, the contribution of each subband state to the probability current can be calculated by

$$j_x^{(j)}(x,t) = \frac{\hbar}{2m_e i}\left(\bar{P}_j^*\frac{\partial}{\partial x}\bar{P}_j - \bar{P}_j\frac{\partial}{\partial x}\bar{P}_j^*\right), \tag{7}$$

where $\bar{P}_j(x,t) = \langle\phi_j|\Psi\rangle$ gives the time-dependent wave function within the j-th subband. Notice that since $\bar{P}_j(x,t)$ is not normalized, its value can be larger than one. Finally, the time-dependent probability current at x_i is given by

$$J_t(x_i,t) = \int_{-\infty}^{+\infty} J_x(x_i,y,t)dy. \quad (8)$$

Solution of Eqs. (6)–(8) forms the basis to understand the conductivity and the trajectory of the wave packet through the wires.

III. RESULTS AND DISCUSSION

For all cases considered in this work, we consider material parameters for InGaAs (wire) and GaAs (barrier material), in which the conduction band of the InGaAs/GaAs heterostructure has a band-offset of 600 meV. Moreover, for InGaAs, the electron effective mass is $m_e = 0.041\ m_0$.[30] The wave packets are injected from left to right at $t = 0$, in the lowest subband $\phi_{n=1}(y)$. Three different values of the kinetic energy of the wave packets are considered: $\varepsilon_1 = 70$ meV, $\varepsilon_2 = 140$ meV, and $\varepsilon_3 = 200$ meV.

Transmission and reflection probabilities obtained with our method are presented in Figs. 2 and 3 as function of the distance W_2 for $L = W_1$ and $L = 2W_1$, respectively. The transmission probabilities are calculated on the left-bottom wire T_1 (green, dashed dotted line), right-output wire T_2 (black, solid line), and right-top wire T_3 (red, dashed line). The reflection R (blue, dashed dotted dotted line) is calculated on the input left-wire. We checked numerically that the sum $R + \sum T_i = 1$ is satisfied up to a maximum error of 0.1%. For a wave packet with kinetic energy ε_1 (Figs. 2(a) and 3(a)), the transmission coefficient T_2 decreases faster than the one with kinetic energy ε_3 (Figs. 2(c) and 3(c)), i.e., the tunnelling through the barrier W_2 is in general larger for higher kinetic energy. Furthermore, the transmission T_2 decreases towards zero with increasing width W_2, and as a consequence, the transmission T_1 and reflection R increase such that $T_1 + R \simeq 1$ for wide W_2. The tunnelling T_3 towards the top-right side is less than 10%, but nonzero even for high kinetic energy of the wave packet and for different W_2 distance. This behavior is shown in Figs. 2 and 3 by red dashed lines for $L = W_1$ and $L = 2W_1$, respectively, and occurs because the quantum wire shape spreads the wave function around the position $x = 0$, specially for $W_2 \to 0$, where the transmission is about 70% through T_1 and the other 30% is reflected R or tunnel through T_2 and T_3, as shown in Fig. 3(c). Tunnelling of wave functions starting in the first excited subband of the input lead is demonstrated to be much lower, though, as shown in Figs. 2(d) and 3(d), where T_2 reaches a maximum value of ≈10%, whereas most of the wave packet (≈75% for small W_2 in both cases) goes through the input (left) wire towards the left-bottom lead 1, as a small part of it (≈10% for small W_2 in both cases) is reflected back (T_3 gives a small contribution ≈5%, as usual). The transmission probability T_2 in Figs. 2 and 3 is perfectly fitted by an exponential function $f(W_2) = A_0 \exp(-W_2/\tau) - A_1$, where τ, A_0, and A_1 are fitting parameters given in Table I.

Let us now discuss the contribution of each subband of the output lead to its overall current. In order to have a better understanding of this problem, we display in Fig. 4(a) the eigenenergies of the output lead as a function of its width. The average wave vector k_x^i of the wave packet is schematically shown in Fig. 4(b) for $L = W_1/2$, in Fig. 4(c) for $L = W_1$, and in Fig. 4(d) for $L = 2W_1$. Here, the highest kinetic energy was chosen to cover the first three subbands in the output lead, where the bottom of the subband is found to be around ε_3, for an output width of $L = 2W_1$. This kinetic energy allows us to calculate the influence of the subbands on the scattering of the wave packet. The number of k_x values allowed for each kinetic energy ε, at different subbands, depends on the width L: for instance, in the case illustrated in Fig. 4(b), when $L = W_1/2$, only $k_3^{(1)}$ is allowed. However,

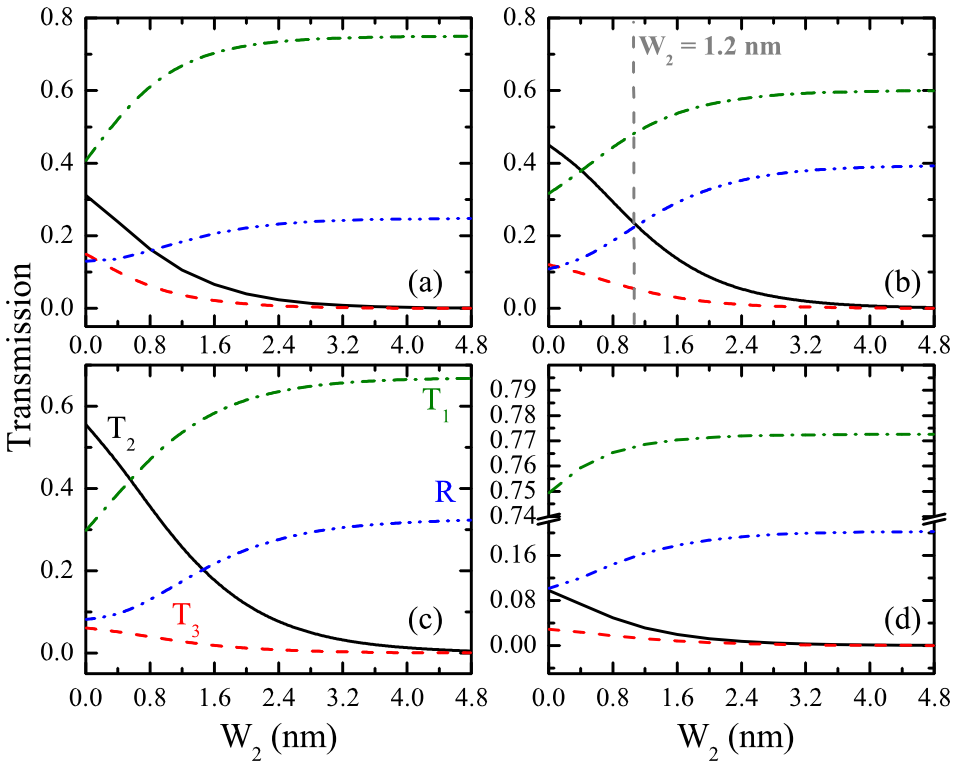

FIG. 2. (a)–(c) Wave packet transmission (T) and reflection (R) probabilities as a function of W_2 for a well width $L = W_1$. The transmission probabilities are calculated in three different points of the QWs: bottom T_1 (green, dashed dotted line), top T_3 (red, dashed line), right T_2 (black, solid line), while the reflection R (blue, dashed dotted dotted line) is calculated at the left side. The wave packet energies are (a) ε_1, (b) ε_2, and (c) ε_3 (propagated on ground state), and (d) ε_3 (propagated on first excited state).

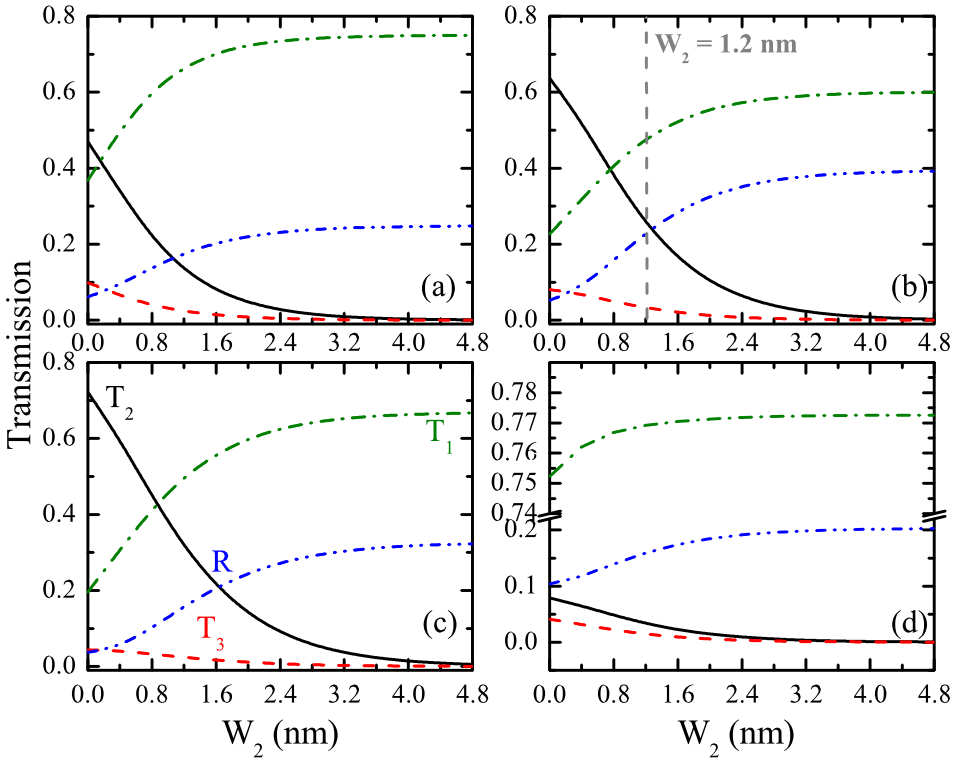

FIG. 3. The same as in Fig. 2, but now for $L = 2W_1$.

TABLE I. Exponential fitting to transmission probabilities T_2 shown in Figs. 2 and 3, for different energies ε and widths of the second wire L.

	$L = 10$ nm			$L = 20$ nm		
ε	A_0	τ	A_1	A_0	τ	A_1
ε_1	0.33	11.46	0.01	0.49	9.89	0.01
ε_2	0.512	15.108	0.035	0.70	13.32	0.03
ε_3	0.620	15.384	0.038	0.80	14.65	0.04
$\varepsilon_3^{(1)}$	0.103	10.979	0.003	0.09	14.12	0.005

this kinetic energy may take values $k_3^{(1)}$, $k_3^{(2)}$, and $k_3^{(3)}$ for ε_3 with $L = 2W_1$ (see Fig. 4(d)). As for our Gaussian wave packet, the initial wave function is a distribution of k_x's around $k_x^{(i)}$ that yields an energy distribution ΔE, as illustrated in Fig. 4(d). More details regarding the initial wave package width in k_x-space can be obtained by Fourier transform and this is explained in detail in Ref. 23. In the case proposed here, where the wave function is also Gaussian in reciprocal space, it is possible to determine the energy distribution of the wave packet as $\Delta E = \hbar^2 k_0 \Delta k / m_e$, where $\Delta k = 2\sqrt{2\ln 2}/\sigma_x$ is the full width at half maximum (FWHM).[23]

Figures 5(a) and 5(b) show snapshots of the wave function with kinetic energy ε_2, calculated at $t = 160$ fs for $W_2 = 1.2$ nm, as indicated by the vertical dashed-gray lines in Fig. 2(b) (for $L = W_1$) and in Fig. 3(b) (for $L = 2W_1$), respectively. It is easy to verify that the wavefunction indeed leaks towards both the horizontal and vertical arms (labelled as 2 and 3 in Fig. 1, respectively) of the right channel,

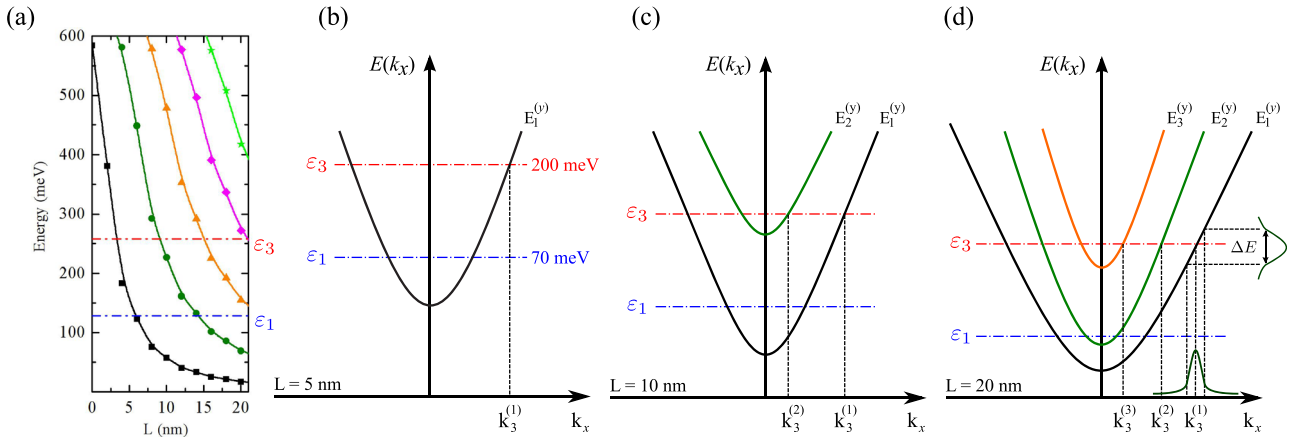

FIG. 4. (a) Bottom energy of the different subbands as function of the quantum well width L. Schematic diagrams that represent the subband energies as function of the wave vector k_x in the x direction are shown for different output wire widths: (b) $L = 5$ nm, (c) $L = 10$ nm, and (d) $L = 20$ nm. The horizontal dashed-dotted lines represent the average energy of the wave packets ε_1 and ε_3.

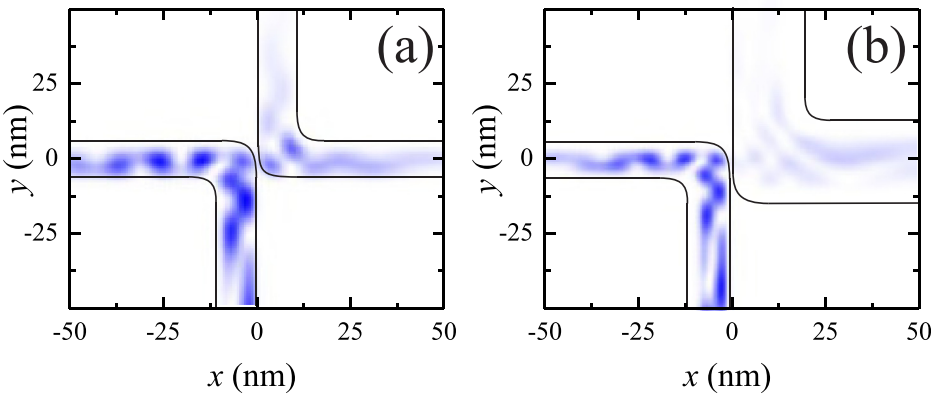

FIG. 5. Snapshot of the wave function at $t = 160$ fs for (a) $L = W_1$ and (b) $L = 2W_1$. The distance between wires is assumed $W_2 = 1.2$ nm, as depicted by the vertical dashed line in Figs. 2 and 3(b), and the wave packet energy is ε_2 in both cases.

leading to the non-zero transmission probabilities T_2 and T_3. Moreover, a tail of the energy distribution around $\varepsilon_2 = 140$ meV has energy higher than the bottom of the second subband of the $L = W_1$ channel, and the snapshot in Fig. 5(a) reveals that part of the wave packet is scattered to this band just by the shoulder of the wires, as inferred by the wiggling function in the output wires. When the right wire has a larger width, $L = 2W_1$, all of its subbands are lowered and the tunnelled wave packet populates its excited states, as one can see by the several peaks of the wave function in this wire in Fig. 5(b).

In order to clarify the role of the well width L in the output lead on the transmission probabilities, in Fig. 6, we display the transmission coefficient on the right side ($T_2 + T_3$) as function of L for two different wave packet kinetic energies ε_1 (a) and ε_3 (b). Three different W_2 distances were considered, namely, 0 nm (black, solid line), 1.2 nm (red, dashed line), and 2.4 (blue, dotted line). The transmission increases with increasing L which is a consequence of the lowering of the subband energy states in the right side over which the tunnelled wave function can be distributed. For a lower wave packet kinetic energy ε_1, the transmission stays below 20% for W_2 distance above 1.2 nm, and for ε_3, the transmission keeps below 40%.

In Fig. 7, we show the projection of the time-dependent wave packet on the ground (P_1), first-excited (P_2), and second-excited state subband (P_3) of the right-lead. The projections are calculated numerically as function of W_2 at the

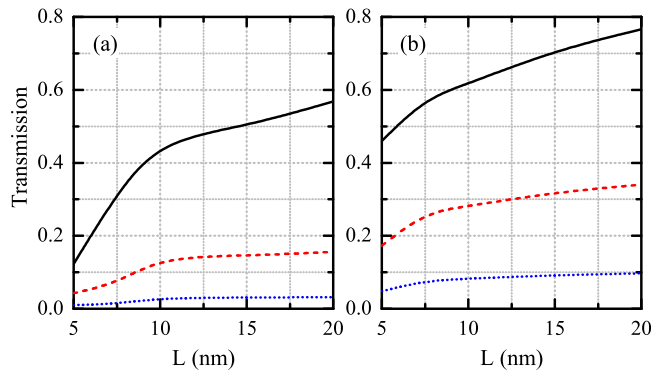

FIG. 6. Transmission coefficient ($T_2 + T_3$) as function of the well width L, for wave packet energies (a) ε_1 and (b) ε_3. Three W_2 distances were considered: 0 nm (black, solid line), 1.2 nm (red, dashed line), and 2.4 nm (blue, dotted line).

point $x = 158$ nm in the right side for output widths $L = W_1$ (a) and $L = 2W_1$ (b). The results are shown for wave packet kinetic energies of ε_1 (black, solid line), ε_2 (red, dashed line), and ε_3 starting in the ground (blue, dotted line) and first excited (green, short dotted) subbands. As expected, all projections decrease towards zero as W_2 increases, since the overall current also exhibits this decreasing behavior. For the narrower leads in Fig. 5(b), the packets with kinetic energies ε_2 and ε_3 scatter to the first excited state ($P_2 \neq 0$), while for energy ε_1, this projection is almost zero for any W_2 value. The projection for the second excited state ($P_3 \neq 0$) is only possible for wave packets with an energy of ε_3, as shown in Fig. 4(c), although still with very small values. For quantum wells with $L = 2W_1$, the subbands energies get closer to each other such that the wave packet scatters to excited states even for energy ε_1, Fig. 7(b).

An analysis of the time-dependent current probability for the wave packet as a function of time is illustrated in Fig. 8. The wave packet propagates from the left to the right side with kinetic energy given by ε_1 (black solid), ε_2 (red dashed), ε_3 in the lowest subband (blue dotted), and ε_3 in the first excited subband (green short-dotted). Around $y = 0$ and along the x-axis, the potential is similar to a simple quantum barrier with height of 600 meV. Calculated at $x = 158$ nm across the potential barrier, the time-dependent current probability is a tunnelling current that can give an estimate about the leakage current through the barrier. In Fig. 8, we plot the tunnelling current probabilities for two different W_2 distances: (a) $W_2 = 0$ nm and (b) 2.4 nm. For each W_2 distance, we consider three different output widths L, from top to bottom: $L = W_1/2$ in the first row, $L = W_1$ in the second, and $L = 2W_1$ in the third row. Clearly, the peak in the probability current is lower at low energies, and it also decreases (increases) with increasing distance (width) W_2 (L). Particularly, in the case of $L = W_1$, Fig. 8 emphasizes the oscillatory behaviour of the probability current for the two distances W_2 used in our calculations. This probability current oscillation is due to wave function scattering in the central region of the wires, as illustrated in Figs. 2 and 3(d). It is easy to see that the current peak occurs faster as the energy increases, as a consequence of the higher Fermi velocity in this case. Although smaller than the other peaks, it is possible to observe that the peak for the wave packet with ε_3 in the first excited subband (green short-dotted) always occurs latter than that for the ground state

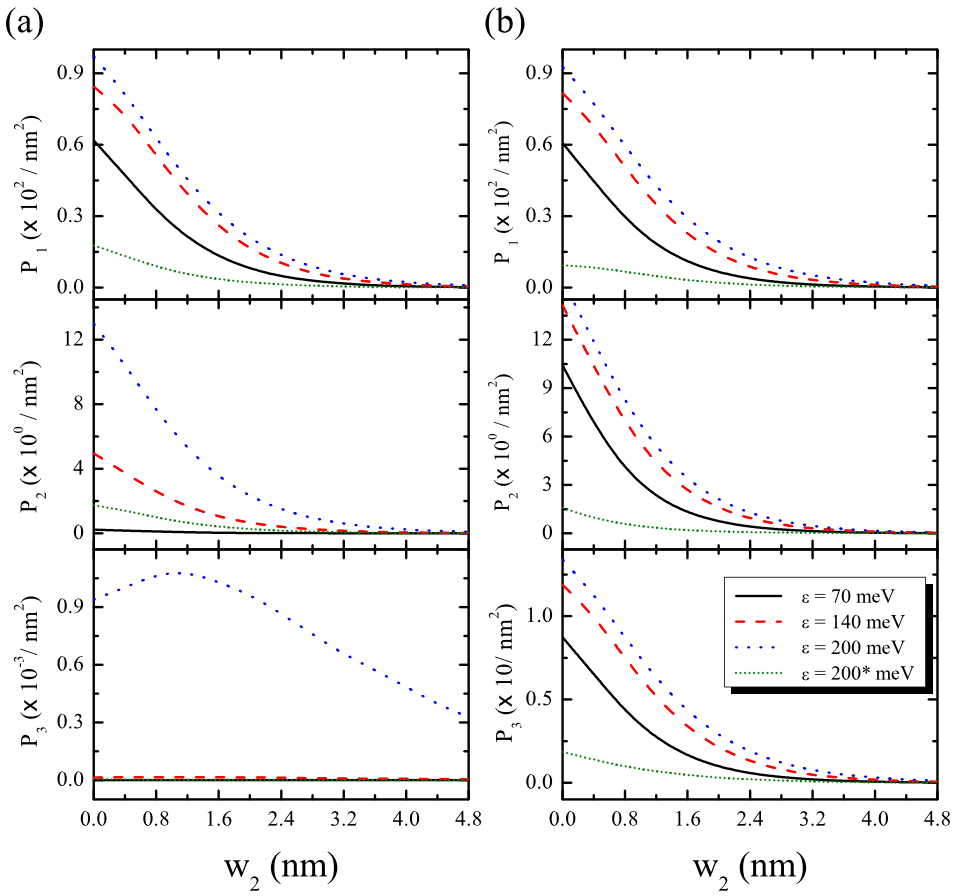

FIG. 7. Projection of the wave function on the ground state P_1, first-excited P_2, and second-excited subbands P_3 integrated in time, calculated at $x = 158$ nm in the right-lead, for output wire widths $L = W_1$ (a) and $L = 2W_1$ (b), as a function of the distance W_2.

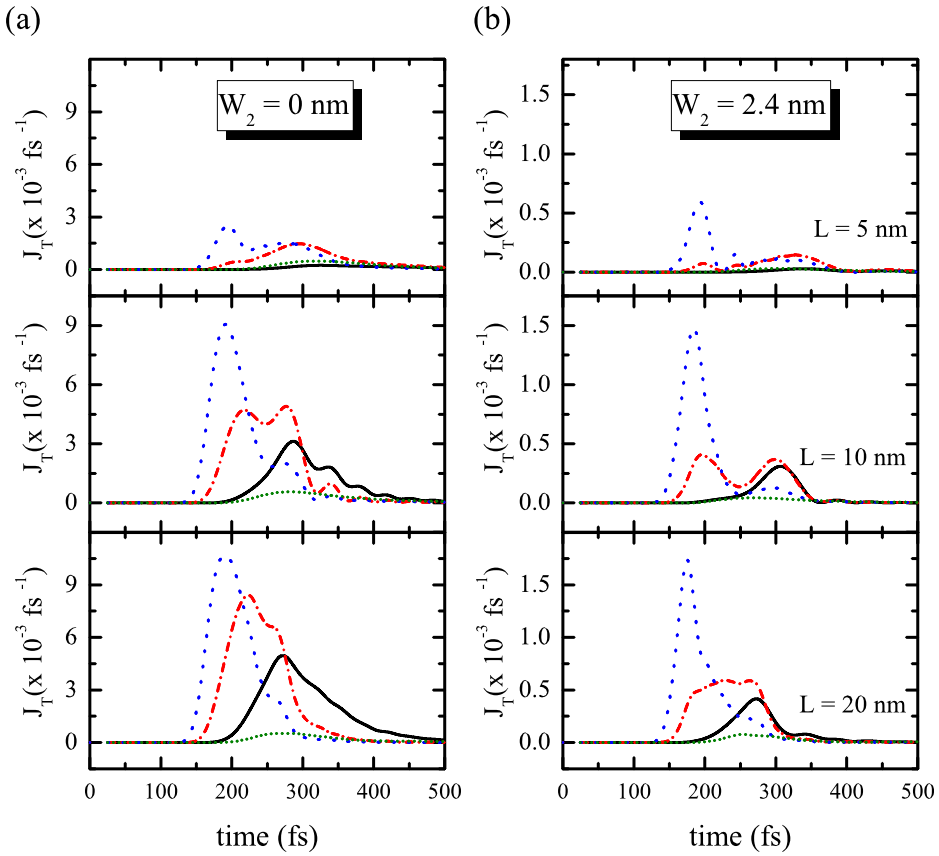

FIG. 8. Total time-dependent probability current for wave packet energies ε_1 (black, solid), ε_2 (red, dashed), ε_3 propagated on the ground state (blue, dotted), and ε_3 propagated on the first excited state (green, short-dotted). Results for different distances W_2 are plotted in columns (a), for $W_2 = 0$ nm, and (b), for $W_2 = 2.4$ nm. The output width L is assumed to be $L = W_1/2$ in the upper row, $L = W_1$ in the middle row, and $L = 2W_1$ in the bottom row.

subband case (blue dotted), since in the former case, the momentum is lower, leading to a lower propagation velocity (see Fig. 5(c)). Besides, increasing L for fixed W_2 slightly shifts the peaks to lower times, which is due to the fact that larger widths lead to lower subband energies and consequently, higher momentum for fixed wave packet energy.

Finally, from a practical point of view, it is important to investigate the behaviour of the conductance for different values of the kinetic energy, W_2 distance, and output width L. With this in mind, we express the conductance as a particular case of the multiband Landauer formalism[32,33]

$$G_l(\varepsilon) = \frac{2e^2}{h}\sum_n T_l^{(n)}(\varepsilon), \tag{9}$$

where the output lead index l is 1, 2, or 3 for conductance calculated with T_1, T_2, and T_3, respectively, and the index n accounts for different occupied subbands in the input lead. The quantum conductance ($G_0 = 2e^2/h$) is used here as unit of electrical conductance, and the transmission coefficients $T^{(n)}_{(x_t,y_t)}(\varepsilon)$ are calculated by setting the wave packet at the initial time in a given subband n, with average energy ε, and integrating the probability current at the axis defined by (x_t, y_t), as in Eq. (4).

Figure 9 displays the conductance G_2 versus the distance W_2 calculated at the right wire (output 2, see Fig. 1) for three wave packet kinetic energies ε_1 (solid black), ε_2 (dashed red), and ε_3 (dotted blue). The conductance was computed by taking into account the transmission probability of the first three subbands for the T_2 coefficient at $x = 158$ nm on the output lead, with output width $L = W_1$ in Fig. 9(a) and $L = 2W_1$ in Fig. 9(b). The conductance depends strongly on the distance W_2. We observe that when the distance W_2 increases, the transmission probability decreases, hence decreasing the conductance in the output region. The wave packet scattering is larger for the case where $L = W_1$, resulting in a larger reflection probability, as can be seen in Figs. 2 and 3, which explains why G is higher in 9(b), as compared to Fig. 9(a). Also, the conductance changes with the kinetic energy of the wave function even for $W_2 = 0$ nm, as observed in Fig. 9(a), as a consequence of quantum scattering at the junction between the wires.

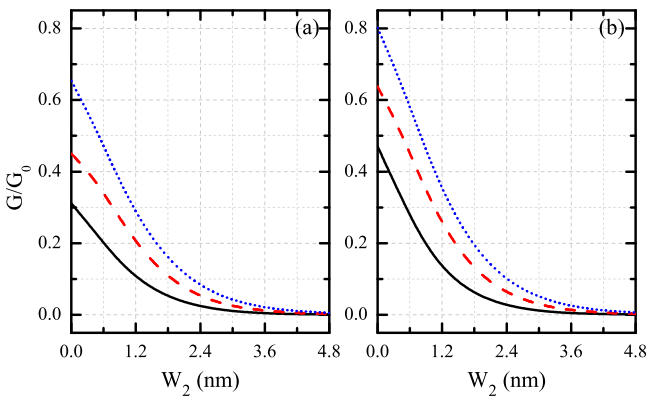

FIG. 9. Conductance G_2 through the output quantum wire as a function of the distance W_2. Wavepacket energy is ε_1 (black, solid lines), ε_2 (red, dashed lines), and ε_3 (blue, dotted lines) for quantum wire widths L (a) 10 nm and (b) 20 nm.

All results presented so far were made for fixed wave packet average energies $\varepsilon = \varepsilon_1$, ε_2, or ε_3. It is important to discuss how these results relate to possible future experiments aiming to verify the quantum tunnelling effects investigated here. In fact, at temperature $T = 0$ K, Landauer formula for conductance is exactly given by Eq. (9), but with transmission probabilities calculated for a plane wave with energy ε. For non-zero temperature, however, the transmission probability must be multiplied by the derivative of the Fermi's energy distribution and then integrated in energy, so that there will be a temperature dependent range of energies around the Fermi level that effectively contribute to the overall conduction. Notice that in our calculations, since we do not consider plane waves, results are never for a single ε and, consequently, they do not describe a zero-temperature situation. Actually, the Gaussian wave packet considered here yields a Gaussian distribution of momenta or, equivalently, a combination of plane waves with different energies. Therefore, in a sense, our results for conductance are closely related to those for non-zero temperature, where the width of the Gaussian wave packet in reciprocal space is related to the width of the energy distribution and, consequently, plays the role of the temperature. Finding the exact relation between temperature and the wave packet width is, however, a difficult task, which is left for future works, whereas here we restrict ourselves to a more qualitative discussion of this matter.

Having stated that we now use our method to calculate the steps in conductance as a function of the electron energy, as expected for a quantum channel, such as the one considered here. These steps cannot be sharp, since we are dealing with a non-zero temperature simulation. This is shown in Fig. 10 for three different values of the W_2 distance: (a) 0 nm, (b) 1.2 nm, and (c) 2.4 nm. The conductance is calculated between the input lead and the three possible output leads, namely, with G_1, G_2, and G_3, showed in Fig. 10 by arrows. Well widths are $L = 5$ nm (red dotted), 10 nm (blue dashed), and 20 nm (black solid). Conductance to the upper lead G_3 is always close to zero and reaches, at most, ≈ 0.15 for $W_2 = 0$, as expected from the low transmission probabilities for this lead observed in previous results in Figs. 2 and 3. Notice that for the widest L width, three subbands are involved in the output lead for a wave packet kinetic energy around ε_3, as shown in Fig. 4(d). On the other hand, for narrow widths, one subband is involved for $L = 5$ nm, Fig. 4(b), and two subbands are involved for $L = 10$ nm, Fig. 4(c). For this reason, the conductances G_2 in Figs. 10(a) and 10(b) are clearly spaced for different values of L. Since G_2 is directly related to the current leak, its increase is responsible for reducing the conductance through the original channel G_1. For lower values of energy ε, conductance G_1 is reduced as the energy increases, due to the increasing current leakage G_2. This effect becomes weaker either as the distance between wires increases or as the second wire width L is made narrower, thus hindering the quantum tunnelling between wires. Furthermore, the differences between conductances G_1 for different values of L become negligible as the W_2 distance becomes too large, see Fig. 10(c). The quantized steps of conductance are also observed in the leakage current G_2, but much lower than those for G_1, which suggests

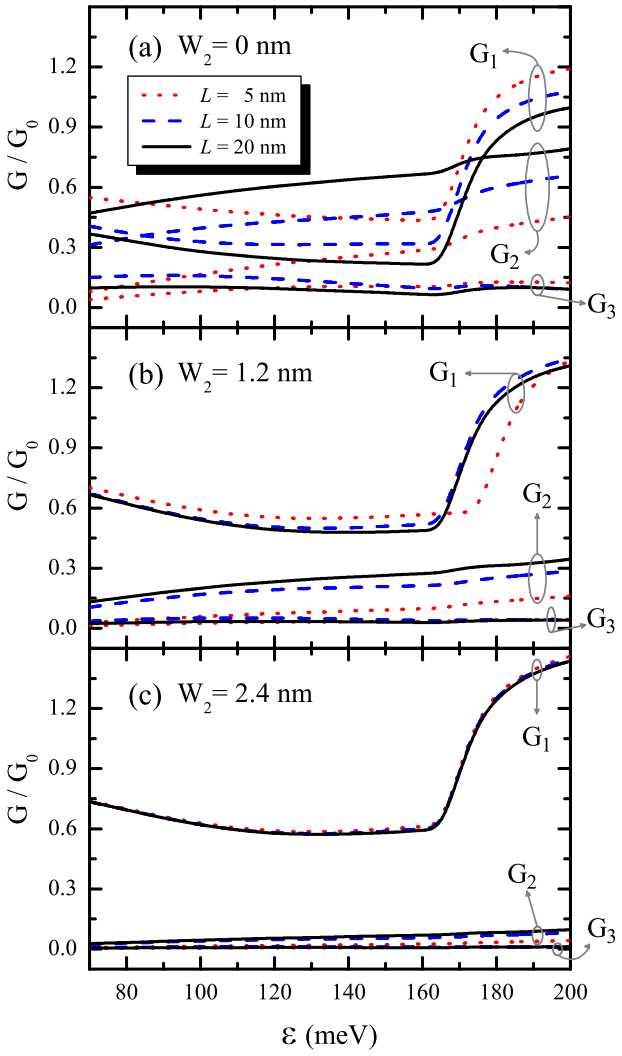

FIG. 10. Conductance through the quantum wire as a function of the kinetic energy of the wave packet, at the three possible output leads, G_1, G_2, and G_3, considering wire widths $L = 5$ nm (dotted red), $L = 10$ nm (dashed blue), and $L = 20$ nm (solid black). The W_2 distance is (a) 0 nm, (b) 1.2 nm, and (c) 2.4 nm.

that states in the first excited subband of the input lead have lower contribution for the leakage current as compared to those coming from the first subband.

IV. CONCLUSIONS

We have presented a theoretical investigation of the electron transmission between two bent quantum wires that is based on the propagation of a Gaussian wave packet. The two L-shaped semiconductor quantum wires are separated by a distance W_2. We showed how a change in the distance between the two QWs W_2 affects the tunneling probability and the time-dependent probability current for different values of kinetic energy wave packet. The wave packet scattered by the potential is reflected and transmitted through the barrier. The tunneling current provides an estimate of the leakage current in the system, which becomes larger as W_2 is reduced. It is of fundamental and practical importance to control these undesired leakage currents in miniaturized electronic devices and circuits, thus, we believe the results presented here might contribute to help future experimental investigations of carrier transport in low dimensional circuits and their future applications in nanotechnology.

ACKNOWLEDGMENTS

A. A. Sousa was financially supported by CAPES, under the PDSE Contract No. BEX 7177/13-5. T. A. S. Pereira was financially supported by PRONEX/CNPq/FAPEMAT 850109/2009 and by CAPES under process BEX 3299/13-9. This work was financially supported by PRONEX/CNPq/FUNCAP, the Science Without Borders program and the bilateral project CNPq-FWO.

[1]A. B. Balantekin and N. Takigawa, Rev. Mod. Phys. **70**, 77 (1998).
[2]R. J. Warburton, C. Schäflein, D. Haft, F. Bickel, A. Lorke, K. Karrai, J. M. Garcia, W. Schoenfeld, and P. M. Petroff, Nature (London) **405**, 926 (2000).
[3]S. S. Mao, Int. J. Nanotechnol. **1**, 42 (2004).
[4]C. Y. Hou, A. Rahmani, A. E. Feiguin, and C. Chamon, Phys. Rev. B **86**, 075451 (2012).
[5]J. J. Ramsey, E. Pan, P. W. Chung, and Z. M. Wang, Nanoscale Res. Lett. **5**, 1272 (2010).
[6]Y. Cohin, O. Mauguin, L. Largeau, G. Patriarche, F. Glas, E. Sondergard, and J. C. Harmand, Nano Lett. **13**, 2743 (2013).
[7]T. Ihn, *Quantum States and Electronic Transport* (Oxford University Press, Oxford, 2010).
[8]H. U. Baranger and A. D. Stone, Phys. Rev. Lett. **63**, 414 (1989).
[9]M. D. Seta, G. Capellini, and F. Evangelisti, Phys. Rev. B **77**, 045431 (2008).
[10]A. Fuhrer, S. Lüscher, T. Ihn, T. Heinzel, K. Ensslin, W. Wegscheider, and M. Bichler, Nature (London) **413**, 822 (2001).
[11]M. T. Björk, B. J. Ohlsson, C. Thelander, A. I. Persson, K. Deppert, L. R. Wallenberg, and L. Samuelson, Appl. Phys. Lett. **81**, 4458 (2002).
[12]T. D. Stanescu, R. M. Lutchyn, and S. Das Sarma, Phys. Rev. B **90**, 085302 (2014).
[13]O. M. Auslaender, A. Yacoby, R. de Picciotto, K. W. Baldwin, L. N. Pfeiffer, and K. W. West, Phys. Rev. Lett. **84**, 1764 (2000).
[14]Y. Tserkovnyak, B. I. Halperin, O. M. Auslaender, and A. Yacoby, Phys. Rev. Lett. **89**, 136805 (2002).
[15]O. M. Auslaender, A. Yacoby, R. de Picciotto, K. W. Baldwin, L. N. Pfeiffer, and K. W. West, Science **295**, 825 (2002).
[16]Y. T. Hou, M. F. Li, Y. Jin, and W. H. Lai, J. Appl. Phys. **91**, 258 (2002).
[17]W. C. Lee and C. Hu, IEEE Trans. Electron. Devices **48**, 1366 (2001).
[18]A. Chaudhry, J. N. Roy, and S. Sangwan, J. Semiconduct. **32**, 054001 (2011).
[19]A. Chaudhry and J. N. Roy, Int. J. Nanoelectron. Mater. **5**, 1 (2012).
[20]A. A. Sousa, A. Chaves, G. A. Farias, and F. M. Peeters, Phys. Rev. B **88**, 245417 (2013).
[21]B. Szafran, Phys. Rev. B **84**, 075336 (2011).
[22]H. Sellier, B. Hackens, M. G. Pala, F. Martins, S. Baltazar, X. Wallart, L. Desplanque, V. Bayot, and S. Huant, Semicond. Sci. Technol. **26**, 064008 (2011).
[23]A. Chaves, G. A. Farias, F. M. Peeters, and B. Szafran, Phys. Rev. B **80**, 125331 (2009).
[24]A. Chaves, G. A. Farias, F. M. Peeters, and R. Ferreira, Commun. Comput. Phys. **17**, 850 (2015).
[25]M. H. Degani, Phys. Rev. B **66**, 233306 (2002).
[26]M. H. Degani and M. Z. Maialle, J. Comput. Theor. Nanosci. **7**, 454 (2010).
[27]A. Alvermann and H. Fehske, Phys. Rev. B **77**, 045125 (2008).
[28]C. Kreisbeck, T. Kramer, S. S. Buchholz, S. F. Fischer, U. Kunze, D. Reuter, and A. D. Wieck, Phys. Rev. B **82**, 165329 (2010).
[29]T. Kramer, AIP Conf. Proc. **1334**, 142 (2011).
[30]B. Hackens, F. Martins, T. Ouisse, H. Sellier, S. Bollaert, X. Wallart, A. Cappy, J. Chevrier, V. Bayot, and S. Huant, Nat. Phys. **2**, 826 (2006).
[31]D. E. Manolopoulos, J. Chem. Phys. **117**, 9552 (2002).
[32]R. Landauer, IBM J. Res. Dev. **1**, 223 (1957).
[33]M. Büttiker, Phys. Rev. Lett. **57**, 1761 (1986).